Nature Communications

https://doi.org/10.1038/s41467-026-73912-5

Article in Press

High-throughput production of microbatteries by a stack-punching method

Received: 19 August 2025

Accepted: 22 May 2026

Cite this article as: Ouyang, Z., Wang, Y., Zhong, Y. *et al.* High-throughput production of microbatteries by a stack-punching method. *Nat Commun* (2026). https://doi.org/10.1038/s41467-026-73912-5

Zhaofeng Ouyang, Yan Wang, Yongyi Zhong, Shitao Geng, Sheza Muqaddas, Shanshan Tang, Bin Yuan, Shuo Wang, Qiuchen Xu, Xiaoju Zhao, Chengqiang Tang, Meng Liao, Peining Chen, Jiawang Liu, Yakun Yuan, Huisheng Peng & Hao Sun

High-throughput production of microbatteries by a stack-punching method

*Zhaofeng Ouyang[1], Yan Wang[1], Yongyi Zhong[2], Shitao Geng[1], Sheza Muqaddas[1], Shanshan Tang[1], Bin Yuan[1], Shuo Wang[1], Qiuchen Xu[1], Xiaoju Zhao[1], Chengqiang Tang[3], Meng Liao[3], Peining Chen[3], Jiawang Liu[1], Yakun Yuan[4], Huisheng Peng[3], and Hao Sun[1]**

[1]*Frontiers Science Center for Transformative Molecules, State Key Laboratory of Synergistic Chem-Bio Synthesis, School of Chemistry and Chemical Engineering, and Zhangjiang Institute for Advanced Study, Shanghai Jiao Tong University, Shanghai 200240, China.*

[2]*Faculty of Mechanical Engineering and Automation, Zhejiang Sci-Tech University, Hangzhou 310018, China.*

[3]*State Key Laboratory of Molecular Engineering of Polymers, Department of Macromolecular Science, and Institute of Fiber Materials and Devices, Fudan University, Shanghai 200438, China.*

[4]*Future Material Innovation Center, School of Materials Science and Engineering, and Zhangjiang Institute for Advanced Study, Shanghai Jiao Tong University, Shanghai 200240, China.*

*Correspondence and requests for materials should be addressed to *H. S.* (*haosun@sjtu.edu.cn*).

Abstract

Microbatteries are critical power sources for integrated circuits, wearable electronics, implantable medical devices, and microrobots. However, their practical applications have been limited by conventional bottom-up assembly methods, which suffer from low production efficiency, poor uniformity, and inferior electrochemical performance. Here we report a top-down stack-punching approach for high-throughput production of microbatteries. Through the integration of an initially anode-free design with an interpenetrating positive electrode|electrolyte fusion layer, we construct robust electrode|electrolyte interfaces to withstand the mechanical stress induced by the high-speed punching process, with a high production rate of 1,800 units per hour. The resulting microbatteries are highly uniform in both physical dimensions and electrochemical performance, achieving a maximum volumetric energy density of 1,306 mWh cm^{-3}, highly competitive among state-of-the-art microbattery technologies. As a proof-of-concept, these microbatteries are integrated with miniature sensors for continuous health monitoring and mounted onto ants and bees to potentially develop biohybrid microsystems for ecological and geological data collection. Overall, our stack-

punching approach offers a promising tool for the large-scale manufacture of high-performance microbatteries, facilitating their translation into next-generation electronic devices and systems.

Introduction

Modern electronic devices are evolving to become smaller, smarter, and more capable (**Fig. 1a**)[1-4]. Millimeter-scale systems can now detect subtle visual, thermal, chemical, and electrical signals, which has significantly expanded their ability to sense and interact with the environment[5-7]. At the heart of these compact systems are microbatteries, which deliver the essential power needed for continuous operation[8,9]. Despite recent advances in microbattery architecture and performance[10,11], their broader implementation remains constrained by manufacturing limitations. Traditional bottom-up assembly methods are generally complex, slow, and difficult to scale, leading to low production efficiency and inconsistent device quality[12-14]. Overcoming these challenges to produce high-performance, uniform microbatteries in a scalable method is critical for their translation into practical applications.

Here we report a top-down stack-punching approach for the high-throughput production of microbatteries. This method integrates an initially anode-free battery architecture with an interpenetrating positive electrode|electrolyte fusion layer (**Fig. 1b**), which stabilizes both the negative electrode|electrolyte and positive electrode|electrolyte interfaces, enabling rapid mechanical punching fabrication without compromising the structural or electrochemical integrity of the devices. The resulting microbatteries exhibited a uniform size and consistent electrochemical performance, delivering a maximum battery-level energy density of 1,306 mWh cm^{-3}. We further demonstrate the broad applicability of these microbatteries in electronic lenses and smart wristbands for continuous health monitoring, as well as biohybrid systems on ants and bees for subtle, mobile environmental sensing. These results highlight the potential of our microbatteries to drive a wide range of next-generation microsystem applications.

Results

Designing microbatteries with high production efficiency and uniformity

To fabricate microbatteries in a consistent and scalable manner, we developed a high-throughput fabrication system (**Fig. 1c**, **d**). In the first step of electrode and electrolyte assembly (Step I), a $LiFePO_4$ positive electrode pre-infiltrated with a polymer electrolyte—comprising lithium bis(trifluoromethanesulfonyl)imide (LiTFSI) and poly(vinylidene fluoride-co-hexafluoropropylene (PVDF-HFP)—was layered between the aluminum (Al) and copper (Cu) foil current collectors (**Fig. 1e**).

This stacked configuration was then subjected to Step II, where individual microbatteries were cut from the large assembly via a high-speed punching process with high efficiency and uniformity (**Fig. 1e**, **f**). The obtained microbatteries were subsequently encapsulated and conveyed for collection in Step III (**Fig. 1e**). This modular punching approach allows flexible adjustment of the battery size from 12 mm to 3 mm simply by changing the puncher size (**Supplementary Fig. 1**), thus offering versatility for diverse applications.

A crucial requirement for this high-speed stack-punching process is the mechanical integrity of the electrode|electrolyte interfaces, which must endure localized stresses without failure. The integration of an initially anode-free configuration with an interpenetrating positive electrode|electrolyte fusion layer ensures the stability of the electrode|electrolyte interfaces (**Fig. 2a**). On the one hand, the stable negative electrode|electrolyte interface was attributed to the film-forming ability of the LiTFSI/PVDF-HFP polymer electrolyte on the Cu foil, which was based on an initially anode-free architecture. On the other hand, the positive electrode|electrolyte interface was further strengthened via a 'dissolving–interpenetrating' strategy. During positive electrode coating in Step I, the *N*-methyl-2-pyrrolidinone (NMP) solvent in the positive electrode slurry partially dissolved the underlying polymer electrolyte membrane, forming a fused interfacial layer at the positive electrode|electrolyte interface (**Fig. 2b**). This fused layer was confirmed by cross-sectional scanning electron microscopy (SEM) and energy-dispersive X-ray spectroscopy (EDS) analyses (**Fig. 2c** and **Supplementary Figs. 2**, **3**). Raman mapping further verified the formation of a compact and continuous interface between the $LiFePO_4$ particle and the polymer electrolyte[15] (**Fig. 2d-f**). This engineered interface significantly improved the mechanical robustness, as confirmed by the well-maintained electrical resistance after 1,000 cycles of bending, stretching, and twisting (**Fig. 2g**). Cross-sectional SEM images further demonstrated that the fused positive electrode|electrolyte interface at central region maintained structural integrity without delamination or cracking after mechanical bending (insets of **Fig. 2g**). The high viscosity of positive electrode slurry and rapid solvent evaporation during fabrication have effectively restricted the diffusion of small-size Super P into the polymer electrolyte layer (**Supplementary Fig. 4**), eliminating the short-circuit risk. In addition, a lower interfacial resistance was verified with the presence of the fusion layer by electrochemical impedance spectroscopy (EIS), indicating facilitated Li-ion transport at the positive electrode|electrolyte interface that benefits the electrochemical performance (**Supplementary Fig. 5**).

Electrochemical performance and consistency

The LiTFSI/PVDF-HFP polymer electrolyte exhibited a wide electrochemical voltage window of 4.78 V (**Supplementary Fig. 6**) and afforded an average Coulombic efficiency of ~99.2% over 300 cycles in a Li||Cu cell at 1 mA cm^{-2} and 1 mAh cm^{-2} (**Supplementary Fig. 7**). At a higher current density of 5 mA cm^{-2} and an areal capacity of 2 mAh cm^{-2}, the Li||Cu cell exhibited stable cycling performance during 50 cycles (**Supplementary Fig. 8**). When paired with a $LiFePO_4$ positive electrode of 3.0 mAh cm^{-2}, the microbattery delivered a discharge capacity of 140 mAh g^{-1} with an overpotential of 85.8 mV at 0.2 C, whereas the discharge capacity of the fusion layer-free microbattery was only 80 mAh g^{-1}, with a significantly larger overpotential of 158.1 mV (**Fig. 3a**). The microbattery also enabled a practical areal capacity of up to 7.7 mAh cm^{-2}, corresponding to an areal energy density of 26.1 mWh cm^{-2} (**Fig. 3b** and **Supplementary Fig. 9**). This can be attributed to efficient Li^+ transport at the positive electrode|electrolyte interface, as evidenced by the high rate capability of 3 C, which retained 78.0% of the capacity retention at 0.1 C (**Fig. 3c**), competitive with commercial thin-film and bulky batteries[16-18]. In comparison, the fusion layer-free microbattery only retained 24.1% of the capacity under the same conditions (**Supplementary Fig. 10**). Nyquist plots showed a lower interfacial resistance and a steeper Warburg slope, indicating enhanced Li^+ diffusion with the presence of the fusion layer (**Supplementary Fig. 5**), which aligned with the enhanced rate performance. At a commercial-level areal capacity of 3.0 mAh cm^{-2}, the microbattery demonstrated stable cycling performance by maintaining 46.0% of its initial capacity after 200 cycles, with an average Coulombic efficiency of ~99.1% (**Fig. 3d** and **Supplementary Fig. 11**). Of course, the cycling stability of these microbatteries should be further promoted to fully meet the requirements in real-world applications.

After 50 cycles in Cu||$LiFePO_4$ microbatteries, the deposited Li maintained a dense and uniform morphology without observable dendrite formation (**Supplementary Fig. 12**), which aligned with the high Coulombic efficiencies and capacity retention. In addition, the stability of the interpenetrating fusion layer at the positive electrode|electrolyte interface after cycling was confirmed by cross-sectional SEM analysis (**Supplementary Fig. 13**), indicating efficient Li^+ transport over battery cycling. This also enabled a 67.9% capacity retention after 50 bending cycles with an average Coulombic efficiency of 97.9% (**Supplementary Fig. 14**). When cycled at an elevated temperature of 50 °C, the cell displayed high cycling stability during 300 cycles with a decent average Coulombic efficiency of 99.0% (**Supplementary Fig. 15**).

To highlight the versatility of the stack-punching approach, we fabricated microbatteries using a high-

energy-density $LiNi_{0.8}Co_{0.1}Mn_{0.1}O_2$ (NCM811) positive electrode. The resulting microbattery exhibited a specific capacity of 170 mAh g^{-1} and retained 84.1% of the original capacity after 20 cycles (**Fig. 3e**, **f**). With a total volume of 1.3 mm^3, the NCM811 microbattery reached a maximum specific energy of 485 Wh kg^{-1} (calculated based on the total mass of the microbattery), competitive with that of state-of-the-art miniature energy storage devices[19-21] (**Fig. 3g** and **Supplementary Table 1**). We further performed laser confocal scanning microscopy (LCSM) to confirm the uniform electrode surface at various diameters from 3 mm to 12 mm (**Supplementary Fig. 16**), demonstrating the decent consistency in microbattery production. More importantly, the stack-punching method ensured high consistency in terms of specific capacity, initial Coulombic efficiency, capacity retention, and thickness across a wide range of device sizes (3 mm to 12 mm in diameter) (**Fig. 3h** and **Supplementary Figs. 17**, **18**). This addresses the challenges of consistency with traditional microbatteries fabricated via conventional bottom-up assembly methods[22,23]. This stack-punching approach enabled the fabrication of 1,800 microbatteries prior to encapsulation within one hour, competitive with that in previous leading reports[20,22,24-29] (**Fig. 3i** and **Supplementary Table 2**). Further advancements in cell stability, packaging, and integration are required to fully meet the requirement for practical microbattery production.

Wearable, on-chip, and biohybrid systems powered by microbatteries

Our microbatteries show promising compatibility with various miniaturized electronic systems. As a proof-of-concept, we integrated a 3-mm microbattery into a smart contact lens to power a miniature tear sensor for real-time monitoring of ocular physiological parameters[30] (**Fig. 4a** and **Supplementary Fig. 19**). The sensors accurately measured the concentrations of potassium (K^+) and sodium (Na^+) ions (**Fig. 4b**, **c**), which are key biomarkers for the early diagnosis of glaucoma and dry eye syndrome, respectively[31-33]. In addition to ocular applications, we used two 3-mm microbatteries in parallel to power a chemical sensor and microcontroller in a wearable wristband (**Fig. 4d**, **e**). For on-chip applications, a high pulse power density is essential to deliver the short bursts of current required for rapid data transmission[34]. Our microbattery exhibited a pulse power density of 2,636 μW mm^{-2} under standard testing conditions (**Supplementary Figs. 20**-**23**), competitive with commercial Ag_2O and Swiss-roll microbatteries[34] (**Fig. 4f** and **Supplementary Fig. 24**). Furthermore, the microbattery could output a discharge voltage greater than 3.40 V for more than 384 hours (**Fig. 4g**), enabling sustained, multiplexed sensing for continuous health monitoring (**Supplementary Fig. 25a**). In addition, our microbatteries show promise in powering autonomous microrobots to monitor harsh environments and to use in search-and-rescue missions (**Fig. 4h** and **Supplementary Fig. 25b**).

We further explored the applications of microbatteries in biohybrid systems. Miniature devices integrated with insects have been proposed as covert, mobile sensors[35-37], but bulky batteries with limited performance have hindered their practical deployment[38]. As a proof-of-concept, we mounted a 3-mm microbattery on an ant (*Camponotus japonicus*) (**Fig. 5a**, **b** and **Supplementary Fig. 26** and **Supplementary Movie 1**). Integrating this microbattery with an optical sensor enabled the monitoring of both individual and collective ant behavior (**Fig. 5c**, **d**). We further equipped a stag beetle (*Lucanidae*) with two parallel microbatteries and a miniature temperature sensor to track variations in the ambient temperature (**Supplementary Fig. 27**). In addition, a bee (*Apis cerana Fabricius*) carried a light-emitting diode (LED) and a microbattery, allowing its flight path to be visualized via emitted light (**Fig. 5e**, **f**). These results highlight the potential of these microbatteries to power lightweight, autonomous systems for covert sensing and environmental monitoring applications across diverse inaccessible locations. Notably, the developed wearable and biohybrid systems are mainly conceptual demonstrations and their practical deployment is future work. Moreover, microbatteries sealed with hot melt tape still require improvements in air tightness and long-term processing reliability to meet the demands of practical, real-world applications (**Supplementary Fig. 28**).

Discussion

In summary, we demonstrated a scalable and versatile stack-punching method for the high-throughput fabrication of microbatteries with a uniform size, structural integrity, and improved electrochemical performance. By integrating an initially anode-free architecture with a fused positive electrode|electrolyte interface, this approach enabled the mass production of microbatteries with a maximum volumetric energy density of 1,306 mWh cm^{-3}, which was highly competitive among state-of-the-art microbatteries. Importantly, this method bridges a critical gap between laboratory-scale microbattery innovation and industrial manufacturing, achieving a production rate of 1,800 units per hour, competitive with that of conventional methods. The modularity and flexibility of the stack-punching method allow straightforward adaptation to fabricate microbatteries of various sizes and positive electrode chemistries, meeting the diverse requirements of miniature electronics, such as wearable health monitors, on-chip electronics, and biohybrid insect-based systems. Our results address the critical challenge of transitioning microbattery technologies from laboratory prototypes to high-throughput production, thereby significantly accelerating their commercial deployment in next-generation electronic devices.

Methods

All insect experiments were approved by the Institutional Animal Care and Use Committee (IACUC) of Shanghai Jiao Tong University and conducted in accordance with the committee's guidelines. The study complied with all relevant ethical regulations and followed the "3R principles" (Replacement, Reduction, Refinement) for animal research.

Materials

Poly(vinylidene fluoride-co-hexafluoropropylene) (PVDF-HFP, 98%, $M_w = 4 \times 10^5$ g/mol, Macklin), 1,3-dioxolane (DOL, 99%, water ≤50 ppm, Adamas), 1,2-dimethoxyethane (DME, 99%, water ≤50 ppm, Adamas), *N*-methyl-2-pyrrolidinone (NMP, 99.5%, water ≤50 ppm, Adamas), *N*,*N*-dimethylformamide (DMF, 99.8%, water ≤50 ppm, Adamas), lithium difluoro(oxalato)borate (LiDFOB, 99.9%, Dodo Chem), lithium tetrafluoroborate ($LiBF_4$, 99.9%, Dodo Chem), diethyl carbonate (DEC, 99.99%, Dodo Chem), fluoroethylene carbonate (FEC, 99.9%, Dodo Chem), and polyvinylidene difluoride (PVDF, 99.5%, $M_w = 1.1 \times 10^6$ g/mol, Solvay 5130) were used as received without further purification. Lithium bis(trifluoromethanesulfonyl)imide (LiTFSI, 98%) was purchased from Adamas and dried under vacuum at 110 °C for 24 hours before use. Lithium nitrate ($LiNO_3$, 99.9%, Nanjing Mojiesi Energy Technology Co., Ltd.), trilayer microporous membranes (Celgard 2325, thickness of 25 μm, polypropylene/polyethylene/polypropylene), and glass fibre membranes (GF/A, thickness of 260 μm, Whatman) were dried under vacuum at 80 °C for 24 hours before use. $LiFePO_4$ powder (99.5%) and super P carbon (99%) were purchased from Shenzhen Kejing Star Technology Co., Ltd. $LiNi_{0.8}Co_{0.1}Mn_{0.1}O_2$ (NCM811, 99%) powder and vapor grown carbon fibre (VGCF, 99.9%) were purchased from Kelude Co., Ltd.

Preparation of the polymer electrolyte membrane

All electrolytes were prepared inside an argon-filled glove box (H_2O < 0.5 ppm, O_2 < 0.5 ppm). PVDF-HFP (0.4 g) and LiTFSI (0.44 g) were added to DMF (5 mL), followed by stirring at 65 °C for 12 hours to obtain a transparent solution. A Celgard 2325 or GF/A separator (5 cm × 5cm) was then dipped into the above solution 5 times and plated onto a clean glass plate for casting with a stainless-steel blade. Finally, the polymer electrolyte membrane was obtained after drying at 80 °C for 15 minutes and then under vacuum at 60 °C for 12 hours to remove residual solvent.

Preparation of positive electrodes with a fusion layer

$LiFePO_4$ powder, super P carbon, and PVDF (93:4:3 w/w/w) were mixed in NMP (solid/liquid ratio of 1:1.2) to obtain a homogeneous slurry. The slurry was drop-coated onto an as-prepared polymer electrolyte membrane using a stainless-steel blade, followed by drying under vacuum at 80 °C for 24 hours to obtain a positive electrode with a fusion layer at the positive electrode|electrolyte interface. The mass loading of the active materials in the positive electrode was regulated by changing the height of the stainless-steel blade, typically ranging from 12 to 55 mg cm^{-2}. For comparison, the fusion layer-free

positive electrode was prepared by casting the $LiFePO_4$ slurry ($LiFePO_4$:Super P:PVDF = 93:4:3 w/w/w) directly onto an Al current collector (thickness of 13 μm, Kelude Co., Ltd.), followed by complete drying under vacuum at 80 °C for 24 hours. The NCM811 positive electrode with a fusion layer was fabricated by mixing NCM811 powder, super P carbon, VGCF, and PVDF (90:4.5:0.5:5 w/w/w/w) via the same method, with a typical mass loading of 35 mg cm^{-2}.

Preparation of the microbatteries

All microbatteries were produced inside an argon-filled glove box (H_2O < 0.5 ppm, O_2 < 0.5 ppm). To prepare microbatteries, a Cu foil (thickness of 4.5 μm, Shenzhen Jingliang), a $LiFePO_4$ or NCM811 positive electrode with a fusion layer, and an Al foil (thickness of 13 μm, Kelude Co., Ltd.) were stacked together and punched into microbatteries of various diameters from 3 mm to 12 mm using our high-throughput punching equipment (Hangzhou Sandi, SD20230720-1, speed of 30 punches per minute, puncher diameter from 3 mm to 12 mm). Five microliters of liquid electrolyte composed of 1 M LiTFSI in DOL/DME (4:1 v/v) with 3 wt% $LiNO_3$ was added to further construct a conformal negative electrode interface, followed by encapsulation of the microbatteries in coin cells (2032 type, grade 316 stainless steel) using a digital pressure controllable electric crimper (MTI, MSK-160E) with a pressure of 0.12 MPa at 25 °C for electrochemical measurements. For the preparation of microbatteries without the fusion layer, the positive electrode and polymer electrolyte membrane were mechanically stacked via the same method. To prepare the Cu||NCM811 microbatteries, a carbonate electrolyte composed of 1 M LiDFOB and 0.2 M $LiBF_4$ in DEC/FEC (2:1 v/v) was prepared as the additional liquid electrolyte. The average microbattery mass of ~3.5 mg was measured by weighing a batch of 50 devices (total mass ~175 mg) using a precision balance (Sartorius, BSA224S-CW, ±0.1 mg accuracy). The fusion layer-free microbatteries were fabricated by stacking and assembling a Cu foil, a bare polymer electrolyte, and a $LiFePO_4$ positive electrode via the same method. For conceptual demonstrations in wearable and on-chip applications, the microbatteries were sealed with hot melt tape (thickness of 100 μm, EQ-PLIB-HMA30, MTI corporation) to minimize the weight of the packaging component. Sealing process was performed at 150 °C under a pressure of 0.3 MPa for 3 s using a commercial heat sealer. The hermeticity of the assembled microbattery was verified by monitoring the open-circuit voltage stability after sealed, which varied by less than 3.5% over 24 hours.

Electrochemical measurements of the microbatteries

All the electrochemical measurements were performed at 25 ± 0.5 °C in a thermostatic test chamber (Neware MHW-200). All the microbatteries were aged for 6 hours before the electrochemical measurements were performed. For Li||Cu cells (2032 type), the galvanostatic Li plating/stripping process was performed at 1 mA cm^{-2} and 1 mAh cm^{-2} or 5 mA cm^{-2} and 2 mAh cm^{-2} using a Neware battery testing system (CT-4008T-5V50mA-164). Linear sweep voltammetry (LSV) was conducted on an electrochemical workstation (CHI660E) at a scan rate of 1 mV s^{-1}. Electrochemical impedance spectroscopy (EIS) measurements were carried out on an electrochemical workstation (CHI660E) in the

frequency range of 1 MHz to 0.01 Hz at 25 °C. The rate and cycling performance of the Cu||$LiFePO_4$ and Cu||NCM811 microbatteries (2032 type) were evaluated using a Neware battery testing system (CT-4008T-5V50mA-164) with voltages ranging from 2.0 to 3.8 V and 2.5 to 4.3 V, respectively. The microbatteries were first operated at 0.1 C for two cycles and then cycled at 0.2 C (1 C = 170 mA g^{-1} for $LiFePO_4$ and 1 C = 200 mA g^{-1} for NCM811). The specific capacities were calculated based on the mass of the active materials (*i.e.*, $LiFePO_4$ or NCM811) in the positive electrode. The specific energy was calculated based on a total mass of 3.5 mg, a capacity of 0.445 mAh, and an average discharge voltage of 3.8 V, with an N/P ratio of 0 due to the initially anode-free configuration. All electrochemical measurements were repeated at least three times to ensure reproducibility. For the pulse power density measurements, the microbattery (2032 type) was charged at different states of charge from 100% to 50%, and a pulse current (from 20 to 5 μA) was applied for 20 s with a time interval of 120 s.

Preparation of integrated devices and biohybrid systems

The K^+ sensor was fabricated by dip-coating carbon nanotubes (CNTs) with a poly(3,4-ethylenedioxythiophene)-poly(styrenesulfonate) (PEDOT:PSS) layer and then a K^+-selective membrane (2 wt% valinomycin, 0.5 wt% sodium tetraphenylborate, 32.7 wt% polyvinyl chloride, and 64.7 wt% bis(2-ethylhexyl) sebacate in 350 μL of cyclohexanone) and drying overnight at 4 °C in the dark[31,39]. For the Na^+ sensor, the Na^+-selective membrane was prepared by dissolving a mixture of Na ionophore X (1%, w/w), Na-TFPB (0.55%, w/w), polyvinyl chloride (33%, w/w) and bis(2-ethylhexyl) sebacate (65.45%, w/w) and dissolved in 660 μL of tetrahydrofuran[31,39]. The remaining steps in the preparation of the Na^+ sensor were the same as those for the K^+ sensor. The Ag/AgCl reference electrode was prepared via cyclic voltammetry. Specifically, the CNTs were sequentially electrodeposited with Ag (7 cycles, −0.9 to 0.9 V at 0.1 V s^{-1} in 5 mM $AgNO_3$/1 M KNO_3 solution) and AgCl (2 cycles, −0.15 to 1.05 V at 0.05 V s^{-1} in 0.1 M KCl/0.01 M HCl solution)[31]. Finally, a Nafion-glutaraldehyde polymer layer was coated on the above Ag/AgCl reference electrodes to stabilize the potential. For microrobot application, a commercial LED lamp was powered by our Cu||$LiFePO_4$ microbattery and loaded on a microrobot with cyanoacrylate glue. The temperature sensor was used to track the variations in temperature of a nearby object[40]. To investigate the individual and collective behaviors of ants (*Camponotus japonicus*), we attached commercial sensors and 3-mm microbatteries to ants with cyanoacrylate glue without impairing their natural movement.

Characterization

Field emission scanning electron microscopy (SEM) was conducted with a Gemini 300 instrument (ZEISS) at an accelerating voltage of 5 kV to characterize the morphology of the $LiFePO_4$ positive electrode|electrolyte interface at 25 °C. Energy dispersive X-ray spectroscopy (EDS) mapping was conducted with an accelerating voltage of 20 kV. Prior to SEM and EDS measurements, the sample was prepared in an argon-filled glovebox (H_2O < 0.5 ppm, O_2 < 0.5 ppm) and quickly transferred to the microscope using an airtight sample holder to avoid air exposure. Raman mapping of the $LiFePO_4$ positive

electrode particles and polymer electrolyte at 25 °C was performed using a Raman microscope (LabRAM Solei, Horiba) with laser excitation at 532 nm. The $LiFePO_4$ positive electrode and polymer electrolyte were identified by their characteristic peaks in the Raman spectra. Observation of electrode surface morphology was carried out by laser confocal scanning microscopy (LCSM, OLS5000, Olympus, Japan). The electrical resistance measurements of the $LiFePO_4$ positive electrode with a fusion layer under different deformation states at 25 °C were performed using a homemade step motor (curvature radius of 2 mm, frequency of 0.8 cycle s^{-1}), and the changes in resistance were recorded using a digital sourcemeter (Keithley 2450) in a two-probe configuration.

Data availability

The data generated in this study are provided in the Supplementary Information. Source data are provided with this paper.

References

1. Armand, M. & Tarascon, J.M. Building better batteries. *Nature* **451**, 652-657 (2008).
2. Zhu, M. & Schmidt, O.G. Tiny robots and sensors need tiny batteries—Here's how to do it. *Nature* **589**, 195-197 (2021).
3. Lee, Y. *et al.* A modular 1 mm^3 die-stacked sensing platform with low power I^2C inter-die communication and multi-modal energy harvesting. *IEEE J. Solid-State Circuits* **48**, 229-243 (2013).
4. Wu, Z. *et al.* Electroluminescence measurement of microscale light-emitting diode wafers using a three-dimensional flexible probe head. *Nat. Electron.* **8**, 496-509 (2025).
5. Zhao, X. *et al.* A self-filtering liquid acoustic sensor for voice recognition. *Nat. Electron.* **7**, 924-932 (2024).
6. Cheng, W. *et al*. Frictionless multiphasic interface for near-ideal aero-elastic pressure sensing. *Nat. Mater.* **22**, 1352-1360 (2023).
7. Mahato, K., Saha, T., Ding, S., Sandhu, S.S., Chang, A.-Y. & Wang, J. Hybrid multimodal wearable sensors for comprehensive health monitoring. *Nat. Electron.* **7**, 735-750 (2024).
8. Zhang, G. *et al.* High energy density picoliter-scale zinc-air microbatteries for colloidal robotics. *Sci. Robot.* **9**, eade4642 (2024).
9. Lu, C. *et al.* High-performance fibre battery with polymer gel electrolyte. *Nature* **629**, 86-91 (2024).
10. Ding, S. *et al.* A fingertip-wearable microgrid system for autonomous energy management and metabolic monitoring. *Nat. Electron.* **7**, 788-799 (2024).
11. Pikul, J.H., Zhang, H.G., Cho, J., Braun, P.V. & King, W.P. High-power lithium ion microbatteries from interdigitated three-dimensional bicontinuous nanoporous electrodes. *Nat. Commun.* **4**, 1732 (2013).
12. Tang, Y., Zhang, Y., Li, W., Ma, B. & Chen, X. Rational material design for ultrafast rechargeable lithium-ion batteries. *Chem. Soc. Rev.* **44**, 5926-5940 (2015).
13. Ouyang, Z., Wang, S., Wang, Y. & Sun, H. Sweat sensing at your fingertips. *Nat. Electron.* **7**, 729-

730 (2024).
14. Kyerematen, N.A., Brousse, T. & Pech, D. Microsupercapacitors as miniaturized energy-storage components for on-chip electronics. *Nat. Nanotechnol.* **12**, 7-15 (2017).
15. Tang, D. *et al.* A multifunctional amino acid enables direct recycling of spent $LiFePO_4$ cathode material. *Adv. Mater.* **36**, 2309722 (2024).
16. Deng, R. *et al.* All-solid-state thin-film lithium-sulfur batteries. *Nano-Micro Lett.* **15**, 73 (2023).
17. Liu, W. *et al.* Designing polymer-in-salt electrolyte and fully infiltrated 3D electrode for integrated solid-state lithium batteries. *Angew. Chem. Int. Ed.* **60**, 12931-12940 (2021).
18. Li, P. *et al.* Swimmable micro-battery for targeted power delivery. *Adv. Funct. Mater.* **34**, 2312188 (2024).
19. Yue, X. *et al.* A nearly packaging-free design paradigm for light, powerful, and energy-dense primary microbatteries. *Adv. Mater.* **33**, 2101760 (2021).
20. Muniraj, V.K.A. *et al.* Bioresorbable and wireless rechargeable implanted Na-ion battery for temporary medical devices. *Adv. Funct. Mater.* **35**, 2417353 (2025).
21. Li, N., Chen, H., Yang, S., Yang, H., Jiao, S. & Song, W.-L. Bidirectional planar flexible snake-origami batteries. *Adv. Sci.* **8**, 2101372 (2021).
22. Ke, B. *et al.* Low-temperature flexible integration of all-solid-state thin-film lithium batteries enabled by spin-coating electrode architecture. *Adv. Energy Mater.* **14**, 2303757 (2024).
23. Ke, B. *et al.* Tape-casting electrode architecture permits low-temperature manufacturing of all-solid-state thin-film microbatteries. *Interdiscip. Mater.* **3**, 621-631 (2024).
24. Ke, B. & Wang, X. Integratable all-solid-state thin-film microbatteries. *Proc. Natl. Acad. Sci.* **122**, e2415693122 (2025).
25. Wei, T.-S., Ahn, B.Y., Grotto, J. & Lewis, J.A. 3D printing of customized Li-ion batteries with thick electrodes. *Adv. Mater.* **30**, 1703027 (2018).
26. Liu, X. *et al.* Integrating aperiodic 3D porous electrodes into 3D batteries through spray-deposited polymer electrolytes. *Adv. Energy Mater.* **14**, 2401330 (2024).
27. Yang, W. *et al.* 3D macroporous frame based microbattery with ultrahigh capacity, energy density, and integrability. *Adv. Energy Mater.* **13**, 2300574 (2023).
28. Zhang, X. *et al.* Fully printed and sweat-activated micro-batteries with lattice-match Zn/MoS_2 anode for long-duration wearables. *Adv. Mater.* **36**, 2412844 (2024).
29. Wang, X. *et al.* Scalable fabrication of printed $Zn//MnO_2$ planar micro-batteries with high volumetric energy density and exceptional safety. *Natl. Sci. Rev.* **7**, 64-72 (2020).
30. Park, J. *et al.* Soft, smart contact lenses with integrations of wireless circuits, glucose sensors, and displays. *Sci. Adv.* **4**, eaap9841 (2018).
31. Wang, L. *et al.* Functionalized helical fibre bundles of carbon nanotubes as electrochemical sensors for long-term in vivo monitoring of multiple disease biomarkers. *Nat. Biomed. Eng.* **4**, 159-171 (2020).
32. He, W. *et al.* Integrated textile sensor patch for real-time and multiplex sweat analysis. *Sci. Adv.* **5**,

eaax0649 (2019).
33. Sempionatto, J.R. *et al.* Eyeglasses-based tear biosensing system: Non-invasive detection of alcohol, vitamins and glucose. *Biosens. Bioelectron.* **137**, 161-170 (2019).
34. Qu, Z. *et al.* A sub-square-millimeter microbattery with milliampere-hour-level footprint capacity. *Adv. Energy Mater.* **12**, 2200714 (2022).
35. Vo-Doan, T.T., Titov, V.V., Harrap, M.J.M., Lochner, S. & Straw, A.D. High-resolution outdoor videography of insects using Fast Lock-On tracking. *Sci. Robot.* **9**, eadm7689 (2024).
36. Iyer, V., Najafi, A., James, J., Fuller, S. & Gollakota, S. Wireless steerable vision for live insects and insect-scale robots. *Sci. Robot.* **5**, eabb0839 (2020).
37. Bai, Y. *et al.* Swarm navigation of cyborg-insects in unknown obstructed soft terrain. *Nat. Commun.* **16**, 221 (2025).
38. Wang, M. *et al.* Biomorphic structural batteries for robotics. *Sci. Robot.* **5**, eaba1912 (2020).
39. Gao, W. *et al.* Fully integrated wearable sensor arrays for multiplexed in situ perspiration analysis. *Nature* **529**, 509-514 (2016).
40. Zhang, S. *et al.* Biomimetic spinning of soft functional fibres via spontaneous phase separation. *Nat. Electron.* **6**, 338-348 (2023).

Funding

H.S. discloses support for the research of this work from National Natural Science Foundation of China (22575145), Scientific Research Innovation Capability Support Project for Young Faculty (SRICSPYF-ZY2025049), Fundamental Research Funds for the Central Universities (25X010202131), Autonomous Project of State Key Laboratory of Synergistic Chem-Bio Synthesis (sklscbs202557) and LUI Che Woo Talent Development Fund (LCW-ZIAS-2026B05).

Acknowledgments

We thank Linlin Ma for the support in Raman measurement and Zhongqiu Bao, Yuanxin Lin, Fen Li, and Fengxiang Dai for their support in scanning electron microscopy measurements.

Author Contributions

H. S. conceived and designed the research project. Z. O. performed electrode and electrolyte preparation, battery production and electrochemical measurements. Z. O. and Y. W. analyzed the electrochemical data. Y. Z. performed the experiments on integrated systems. S. G. and S. M. performed the scanning electron microscopy measurements. S. T. and B. Y. performed the Raman spectroscopy measurements. S. W., Q. X., X. Z., C. T., J. L., and Y. Y. prepared the sensors and wearable devices. Z. O., M. L., P. C., H. P., and H. S. prepared the manuscript. All the authors participated in the data analysis and discussion.

Competing interests

The authors declare no competing interests.

Supplementary Information is available for this paper.

Correspondence and requests for materials should be addressed to H. S. (haosun@sjtu.edu.cn).

Figures

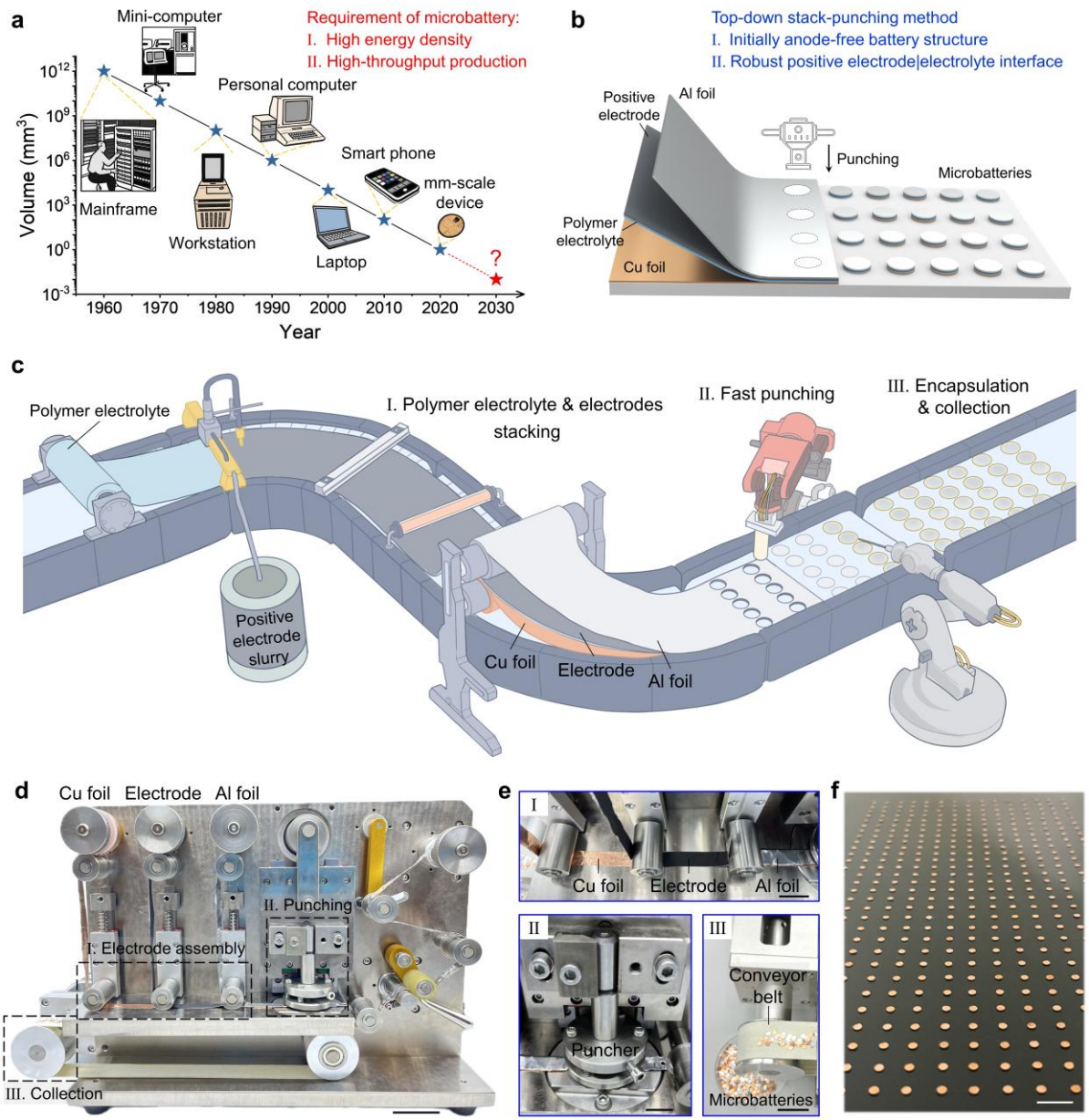

Fig. 1 | High-throughput production of microbatteries by a top-down stack-punching method. a, Evolution of microsized computing devices on the basis of Bell's Law[3]. **b**, **c**, Schematic illustration of the top-down stack-punching strategy (**b**) and the detailed fabrication procedures (**c**) for high-throughput microbattery production. **d**, **e**, Photographs of the customized equipment (**d**) and three main procedures (**e**), including (I) electrode assembly, (II) fast punching, and (III) encapsulation and collection. **f**, Photograph of a 15 × 30 array of 3-mm microbatteries produced by the top-down stack-punching method.

Scale bars, 10 cm (**d**); 20 mm (**e**); and 10 mm (**f**).

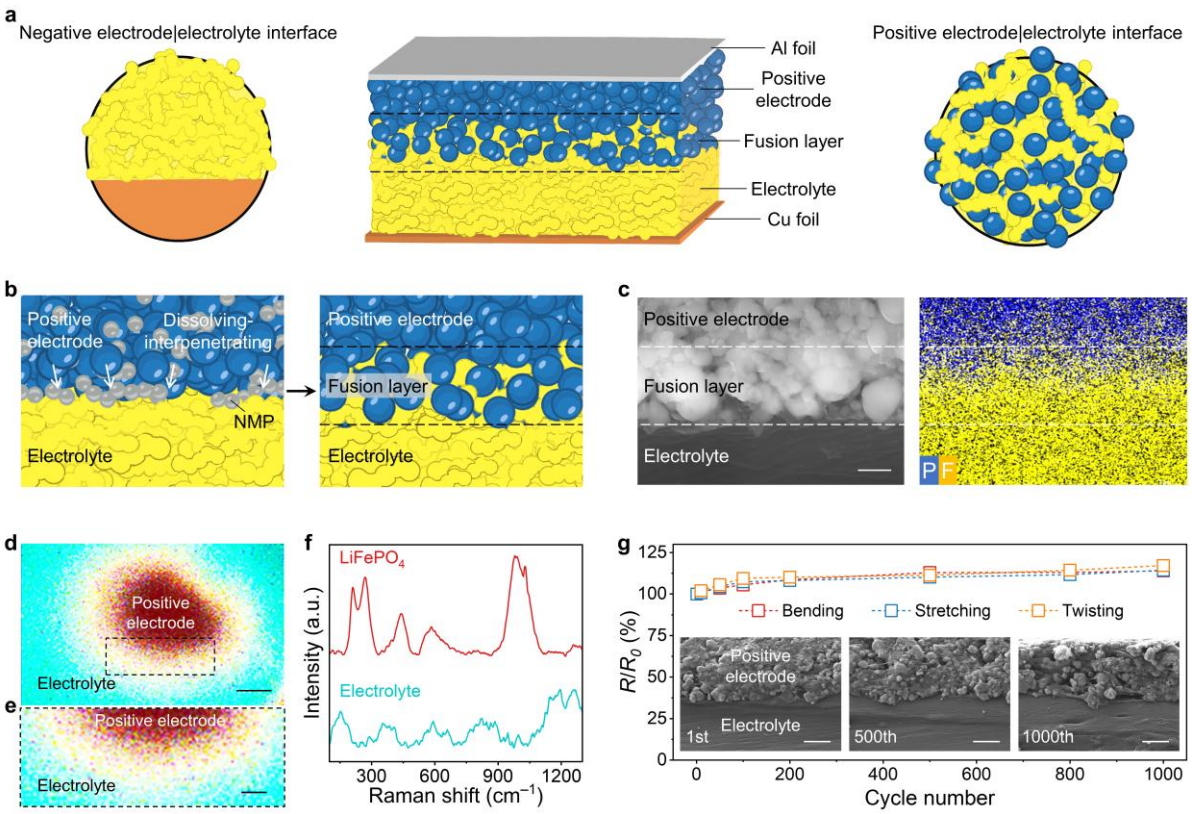

Fig. 2 | Interfacial design of stable electrode|electrolyte interfaces. a, Schematic illustration of negative electrode|electrolyte and positive electrode|electrolyte interfaces that can accommodate the high-speed stack-punching process. **b**, Schematic illustration of fusion layer formation at the positive electrode|electrolyte interface via a 'dissolving–interpenetrating' effect. **c**, Cross-sectional SEM image and the corresponding EDS elemental mapping profile of the positive electrode|electrolyte interface. **d**, **e**, Raman mapping images of the positive electrode|electrolyte interface at different magnifications. **f**, Corresponding Raman spectra of the $LiFePO_4$ positive electrode and polymer electrolyte. **g**, Variation in the two-probe electrical resistance of the $LiFePO_4$ positive electrode with a fusion layer under bending, stretching, and twisting. R_0 and R represent the two-probe electrical resistances before and after deformation, respectively. The insets show cross-sectional SEM images of the positive electrode|electrolyte interface at central region at the 1st, 500th, and 1,000th bending cycles. All characterizations were performed on as-prepared $LiFePO_4$ positive electrode with a fusion layer at 25 °C without electrochemical cycling. Scale bars, 500 nm (**c**); 1 μm (**d**); 500 nm (**e**); and 2 μm (**g**).

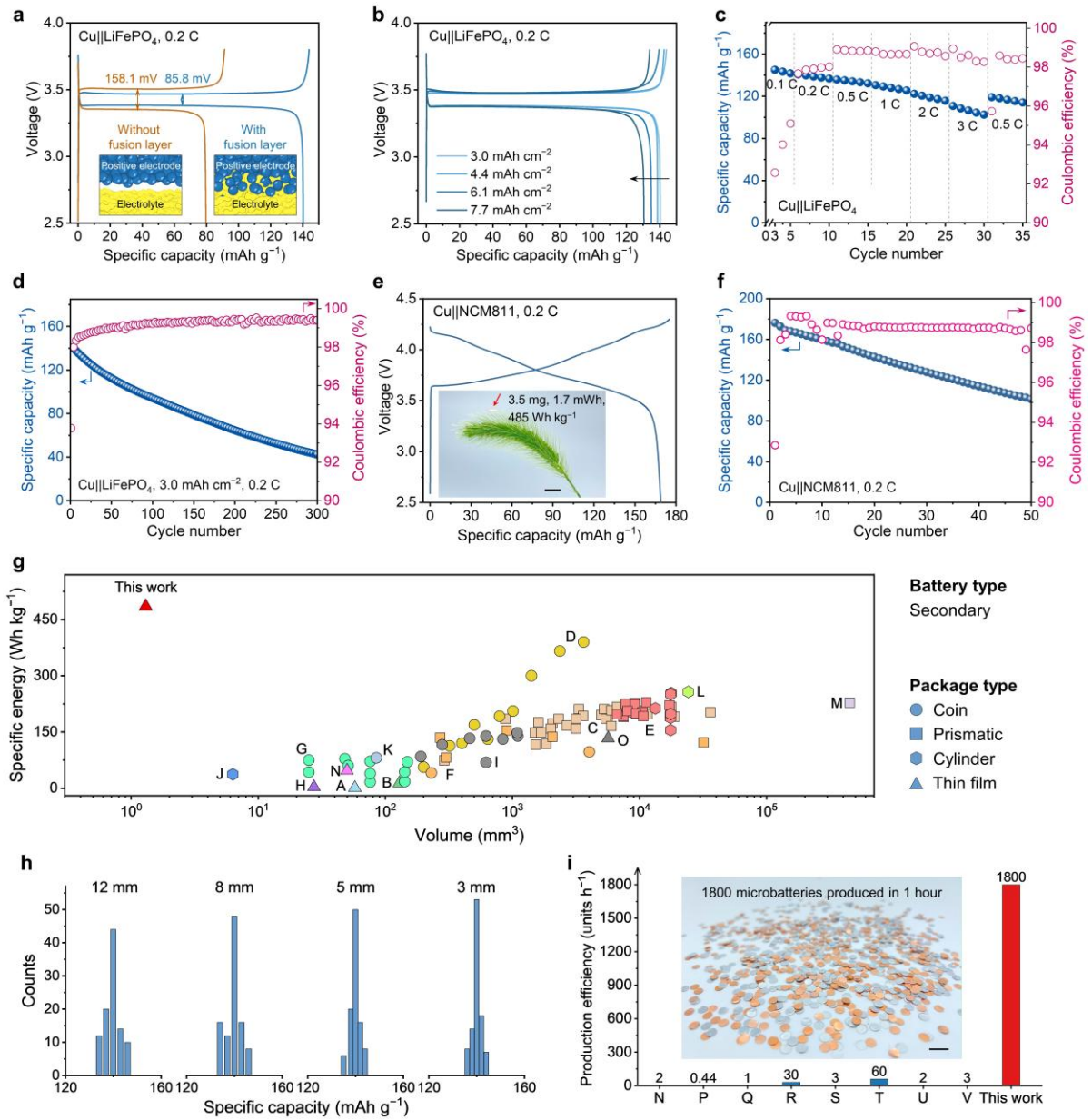

Fig. 3 | High electrochemical performance and consistency of the high-throughput-produced microbatteries. a, Galvanostatic charge–discharge curves of 3-mm microbatteries with and without a fusion layer. The areal capacity of $LiFePO_4$ is 3.0 mAh cm^{-2}, and the charge–discharge rate is 0.2 C (1 C = 170 mA g^{-1} for $LiFePO_4$) unless otherwise specified. **b**, Galvanostatic charge–discharge curves of the 3-mm microbattery at various areal capacities from 3.0 to 7.7 mAh cm^{-2}. **c**, Rate performance of the 3-mm microbattery at increasing rates from 0.1 C to 3 C. **d**, Cycling performance of the 3-mm microbattery over 300 cycles. **e**, Galvanostatic charge–discharge curves of a 3-mm microbattery using an NCM811 positive electrode at 0.2 C (1 C = 200 mA g^{-1} for NCM811). The inset shows a 3-mm microbattery with

a total mass of 3.5 mg placed on a *Setaria viridis* individual. Scale bar, 5 mm. **f**, Cycling performance of a 3-mm microbattery using an NCM811 positive electrode for 50 cycles. The areal capacity of NCM811 in **e** and **f** is 6.3 mAh cm^{-2}. **g**, Comparison of the specific energy and volume of our microbattery with those of state-of-the-art rechargeable microbatteries. A-M: Ref. 19, N: Ref. 20, O: Ref. 21. See **Supplementary Table 1** for detailed comparison data. **h**, Distributions of the specific capacities of 400 microbatteries with various diameters ranging from 12 mm to 3 mm. **i**, Comparison of the production efficiency of our device and previously reported miniature energy storage devices. The inset shows 1,800 microbatteries produced in 1 hour. Scale bar, 5 mm. N: Ref. 20, P: Ref. 24, Q: Ref. 25, R: Ref. 26, S: Ref. 22, T: Ref. 27, U: Ref. 28, V: Ref. 29. See **Supplementary Table 2** for detailed comparison data.

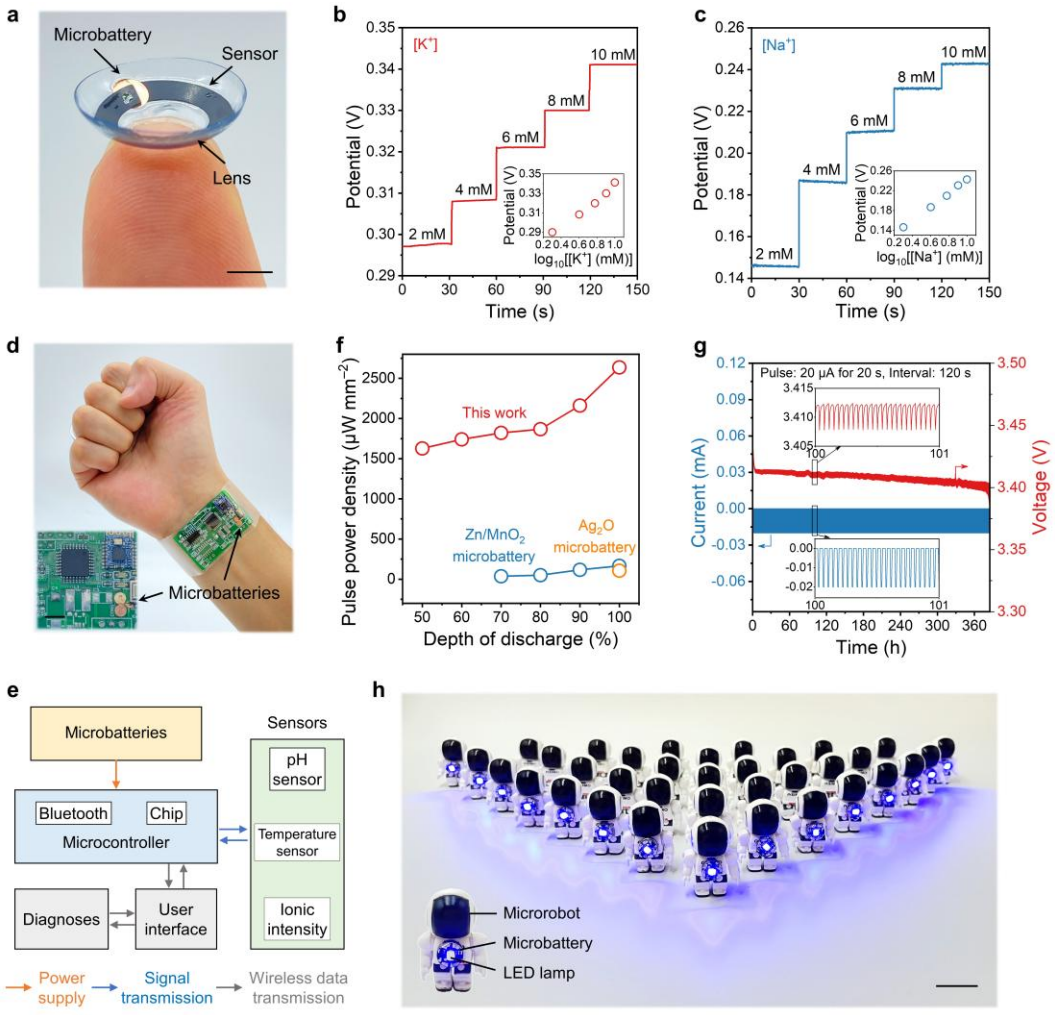

Fig. 4 | Wearable and on-chip applications of the high-throughput-produced microbatteries. a, Conceptual demonstration of a smart lens composed of a miniature sensor and a 3-mm microbattery on a fingertip. Scale bar, 5 mm. **b**, **c**, Open-circuit potential responses of a K^+ sensor (**b**) and Na^+ sensor (**c**). The insets show the calibration curves at different concentrations of K^+ and Na^+. **d**, Conceptual demonstration of a smart wristband with two parallel microbatteries as the power source. Scale bar, 5 mm. **e**, Block diagram of a wearable system integrating multiple sensors and microcontroller powered by microbatteries. Physiological data are continuously collected and transmitted to a user interface for monitoring and diagnostic purposes. **f**, Comparison of pulse power densities at different depths of discharge for our microbattery and previously reported microbattery systems. **g**, Change in voltage as a function of time with a pulse current of 20 μA for 20 s and standby for 120 s at a depth of discharge of 100%. **h**, Conceptual demonstration of swarm microrobots powered by microbatteries for potential applications. Scale bar, 20 mm.

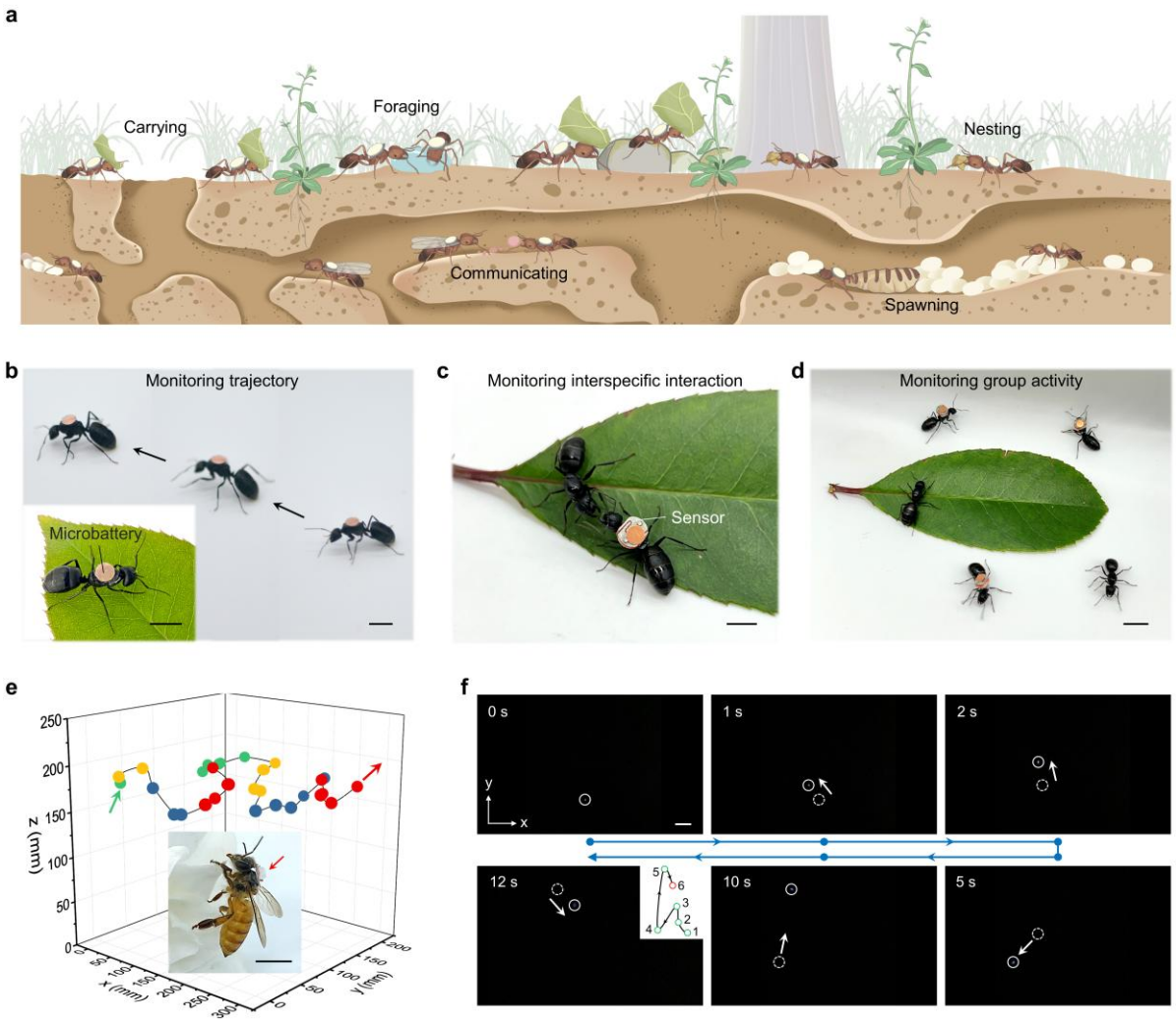

Fig. 5 | Biohybrid systems powered by microbatteries. a, Schematic illustration of ant colony biologging behavior monitoring using miniature sensors powered by high-throughput-produced microbatteries. **b**, Snapshots of an ant carrying a 3-mm microbattery. The inset shows the microbattery-equipped ant on a leaf. Scale bars, 5 mm. **c**, **d**, Conceptual demonstrations of the ant equipped with a microbattery and sensor interacting with other ants for potential monitoring of interspecific interactions (**c**) and group activity (**d**). The scale bars in **c** and **d** are 5 and 10 mm, respectively. **e**, Flight path of a bee carrying an LED lamp powered by a 3-mm microbattery. The inset shows a close-up of the bee with the mounted LED lamp and microbattery. Scale bar, 5 mm. **f**, Video frames of a bee in flight. Scale bar, 20 mm. The inset displays the trajectory of the flying bee.

Editorial Summary:

Microbatteries are essential for miniaturized electronics, but it is currently difficult for scale-up fabrication with high efficiency and high consistency. Here, authors report a stack-punching method that enables high-throughput fabrication of microbatteries with high consistency, demonstrating their potential for wearable devices and biohybrid systems.

Peer Review Information: *Nature Communications* thanks Zhi Li and the other, anonymous, reviewer(s) for their contribution to the peer review of this work. [A peer review file is available.]